Results in Engineering 3 (2019) 100016

Contents lists available at ScienceDirect

Results in Engineering

journal homepage: www.editorialmanager.com/rineng/Default.aspx

Switching arc inversion based on analysis of electromagnetic characteristics

Hongchen Zhao [a,*], Xiaoming Liu [a,b], Gang Wang [c]

[a] School of Electrical Engineering, Shenyang University of Technology, Shenyang, 110870, China
[b] Tianjin Key Laboratory of Advanced Electrical Engineering and Energy Technology, Tianjin, 300387, China
[c] School of Mechanical Engineering, Guizhou Institute of Technology, Guiyang, 550003, China

ARTICLE INFO

Keywords:
Inversion method
MPGA
Switching arc
TGSVD

ABSTRACT

It is difficult to describe the characteristics of an arc in low-voltage switching equipment in terms of its most essential features using conventional arc models. In this paper, arc inversion is introduced to explore a new research approach to examine the nature of low-voltage switching arcs. Based on electromagnetic analysis, the arc is equivalent to a group of threadlike current segments. Then, the arc parameters are obtained by inverting the magnetic data calculated at the sampling point array. The multi-population genetic algorithm (MPGA) is adopted to solve the Biot-Savart operator equations to search the arc position, with the current density inverted by the truncated generalized singular value decomposition (TGSVD), in which the regularization parameter is chosen by the generalized cross-validation (GCV) criterion. The result shows that, by combining the MPGA with TGSVD, both the position and current distribution of an arc can be reconstructed accurately, which can help realize arc control and guide the design of low-voltage switches with improved performance parameters.

Introduction

As a contact switch, an arc is inevitably produced in a circuit breaker during the process of cutting off current. An arc provides a conductive path for the system, but it will affect the switching life of the electrode and arc-extinguishing system. Research on the evolution of the dynamic behavior of arcs in the time domain has an important influence on the breaking capacity and life of switches. Due to the switching arc behavior has spatial nonlinear characteristics, using a numerical experimental method with a conventional measurement method combining the spatial and temporal evolution behavior description of an arc is an effective means of designing high-technology parameter switching of a system. At present, the main method of experimental research on switching arcs includes high-speed charge-coupled-device (CCD) cameras [1], optical fiber array [2] spectroscopy [3], as well as other optically based and magnetic testing methods. The optical testing methods are conceptually simple and feasible to obtain the arc motion and the electron temperature at various moments. For convenience of observation, the chamber walls of the circuit breakers are usually drilled with holes, thus the metallic atoms concentration and plasma temperature can be observed synchronously from the viewpoints. Some scholars presented the magnetic diagnostics, from which the arc motion is obtained by the magnetic sensor array. Toumazet proposed to obtain the arc shape and position from the magnetic diagnostics, combined with the arc volume estimation [4]. Debellut used the magnetic diagnostics to study the re-strike phenomenon of the arc [5]. Zhang proposed to use the intelligent optimization algorithm to invert the arc shape, and verified its effectiveness by experiments [6].

Genetic algorithm (GA) is a highly parallel, stochastic and adaptive global optimization probabilistic search algorithm developed from the evolutionary mechanism of biology. However, the conventional GA often has the shortcoming of premature convergence in solving high-dimensional optimization problems. Compared with GA, the multi-population genetic algorithm (MPGA) avoids the problem of premature convergence through the following improvements: 1) MPGA introduces multiple populations for optimization process, and different populations are given different crossover probability and mutation probability. 2) The migration operator introduces the optimal individual into other populations regularly, which realizes the information exchange among different populations. 3) The optimal individuals of each population are preserved by artificial selection operator in every generation to ensure that the optimal individuals will not be lost.

The MPGA shows more stability and accuracy than GA in many practical applications. Cochran [7] proposed the multi-population genetic algorithm (MPGA) to solve parallel machine scheduling problems. Li used MPGA to calculate the motor parameters in air-coiled permanent

* Corresponding author.
E-mail address: schoolstudyboy@126.com (H. Zhao).

https://doi.org/10.1016/j.rineng.2019.100016
Received 28 February 2019; Received in revised form 19 April 2019; Accepted 20 May 2019

magnetic linear synchronous motors by solving a multi-objective optimization problem [8]. Zhou validated that the MPGA performed better than GA in solving the multi-choice multidimensional knapsack problem [9].

In addition, the regularization methods for ill-posed problems are also efficient for arc current reconstruction. Dong [10] investigated the arc inversion accuracy of Tikhonov regularization with different regularization parameter selection strategies. In Ref. [11], Ghezzi studied the feasibility of the regularization methods based on singular value decomposition for the arc current reconstruction. However, the state-of-the-art regularization methods for arc inversion are all based on the singular value decomposition (SVD) of the operator. It is necessary to explore the improved regularization techniques with higher precision for arc current reconstruction.

Based on the above analysis, we obtain the arc position and current distribution by inverting the magnetic data of the arc. We use the MPGA instead of GA to inverse the arc position. After the arc position is calculated by the nonlinear optimization process of MPGA, the coefficients of the electromagnetic forward equations are determined. To solve these equations from which the coefficients are determined by the MPGA, we use the TGSVD method to reconstruct the current distribution [12]. And the general cross-validation (GCV) criterion is applied to select the regularization parameter. The numerical result shows that the calculation accuracy of TGSVD is far superior to that of truncated singular value decomposition (TSVD). This work is to understand the macroscopic shape and current distribution characteristics of the low-voltage arc by combining the MPGA optimization process with the TGSVD regularization to solve the electromagnetic inverse problems.

Physical mathematical model of low-voltage switching arc

Models and hypotheses

The two-dimensional (2D) model of a simplified circuit breaker in the XOZ coordinate system is shown in Fig. 1. When the contact breaks, the arc between the contacts is elongated, with an increase of the trip. Under the action of the blowing force in the extinguishing chamber, the arc reaches an arbitrary position at a certain time.

To simplify the calculation, it is assumed that the arc occurs in the XOZ plane. In fact, due to the arc running rail and the limitation of the chamber wall, the arc roots move rapidly along the track. In order to obtain the position and shape of the arc, the electrodes, contact, and arc current are assumed as follows: The electrodes, extinguishing grid plates, and contacts are assumed to be a rectilinear thread-like unit; the arc is assumed to be a set of multi-segment current lines. Thus, the magnetic field generated by the simplified arc model can be obtained by the magnetic sampling points array.

Magnetic field of current line element

Based on the Biot-Savart law, the numerical representation of magnetic induction generated by the rectilinear current is derived as follows. Let $A(x_a, y_a, z_a)$ and $B(x_b, y_b, z_b)$be the coordinates of the initial and termination nodes of the current unit, respectively, which is flown by a current j_e; see Fig. 2. EFGH represents the magnetic measuring plane. Let $S(x_s, y_s, z_s)$ denote the position of the magnetic sampling point. Then, the Biot-Savart law yields

$$B(\boldsymbol{r}) = \frac{\mu_0}{4\pi}\int_{AB}\frac{j_e d\boldsymbol{l}\times(\boldsymbol{r}-\boldsymbol{r}_0)}{|\boldsymbol{r}-\boldsymbol{r}_0|^3}, \tag{1}$$

where μ_0 is the permeability of vacuum, $\boldsymbol{r}$ denotes the target point position, and $\boldsymbol{r}_0$ denotes the source point position. The expression (1) is a line integration and solved analytically, i.e., transformed into the format of algebraic equations. Thus the magnetic contribution of each current unit to each sampling point is formed as

$$\boldsymbol{B} = \frac{\mu_0 \boldsymbol{j}_e}{4\pi d_0}(\cos\theta_1 - \cos\theta_2), \tag{2}$$

where d_0, θ_1, and θ_2 are shown in Fig. 2. We suppose the arc current locates in the two-dimensional plane. Then, the magnetic field components B_x, B_y, and B_z at sampling point S can be represented as follows:

$$\boldsymbol{B} = \begin{bmatrix} B_x & B_y & B_z \end{bmatrix}^{\mathrm{T}} = \frac{\mu_0 j_e}{4\pi d_0 \beta}(\cos\theta_1 - \cos\theta_2)\begin{bmatrix}\beta_1\\ \beta_2\\ \beta_3\end{bmatrix}, \tag{3}$$

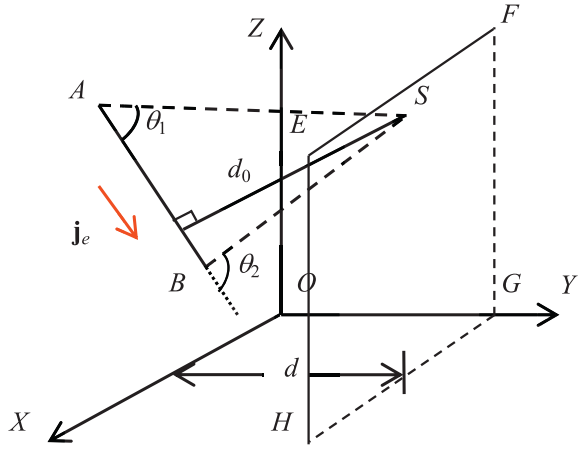

Fig. 2. Rectilinear current unit "AB" and the magnetic measurement plane EFGH.

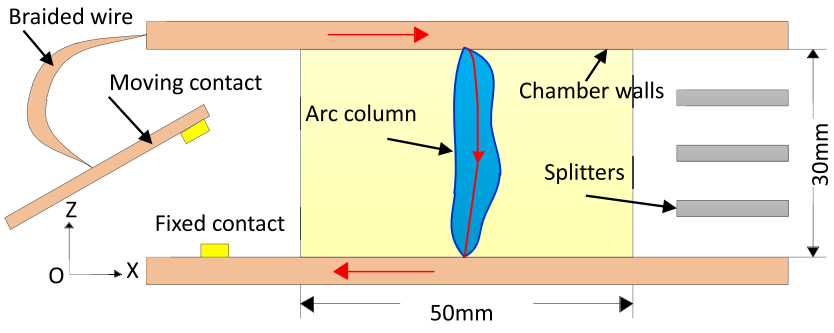

Fig. 1. Arc-breaking system and 2D model of arc.

$$d_0 = \frac{\sqrt{\alpha_1^2 + \alpha_2^2 + \alpha_3^2}}{\sqrt{(x_b - x_a)^2 + (y_b - y_a)^2 + (z_b - z_a)^2}}, \tag{4}$$

$$\beta = \sqrt{\beta_1^2 + \beta_2^2 + \beta_3^2}, \tag{5}$$

where d_0 is the distance between the point S and the current unit. The optimum distance d for the magnetic measurement in Fig. 2 is 5−15 mm, which was validated in Ref. [10]. We set the distance $d = 15$ mm α_1, α_2, α_3, β_1, β_2, and β_3 are the parameters associated with the coordinates of the initial point$A(x_a, y_a, z_a)$, the termination point$B(x_b, y_b, z_b)$, and the sensor point$S(x_s, y_s, z_s)$. These parameters in (3)–(5) are calculated as follows,

$$\overrightarrow{SA} \times \overrightarrow{SB} = \beta_1 \boldsymbol{i} + \beta_2 \boldsymbol{j} + \beta_3 \boldsymbol{k}, \tag{6}$$

$$\overrightarrow{AS} \times \overrightarrow{AB} = \alpha_1 \boldsymbol{i} + \alpha_2 \boldsymbol{j} + \alpha_3 \boldsymbol{k}, \tag{7}$$

$$\cos\theta_1 = \frac{\overrightarrow{AB} \cdot \overrightarrow{AS}}{|\overrightarrow{AB}||\overrightarrow{AS}|}, \cos\theta_2 = \frac{\overrightarrow{BA} \cdot \overrightarrow{BS}}{|\overrightarrow{BA}||\overrightarrow{BS}|}, \tag{8}$$

where $\boldsymbol{i}$, $\boldsymbol{j}$ and $\boldsymbol{k}$ are the unit vectors of the X, Y and Z directions.

According to Refs. [4,5], the number of segments of the current lines should be more than 2. We adopt the three-segment arc model. To simplify the calculation, we only consider the stage of arc moving between the parallel rails in the chamber, denoted region Ω in Fig. 1. We assume that the segment nodes of each current line locate at the trisector between the electrode plates; see Fig. 3. The anode and cathode spots are numbered 1 and 18, respectively. The eight terminal nodes of the first set of segments are numbered 2,3,…,9 and the second set of eight terminal nodes are numbered 10,11,…,17. The length and height of the arc chamber are 50 and 30 mm, respectively. The x-component magnetic field measured in plane EFGH is represented according to formulas (3)–(5). When the distance between electrodes is fixed, the y and z coordinates of each node are known. Thus, the x coordinates $x_1, x_2, \ldots, x_{18}$ of each node must be solved to search for the arc position. We arrange $m = 11 \times 7$ sensor points (see Fig. 3) and at each point a nonlinear equation is formed, with the equations represented as follows:

$$\begin{bmatrix} a_{11} & \cdots & a_{1n} \\ \vdots & & \vdots \\ a_{m1} & \cdots & a_{mn} \end{bmatrix} \begin{pmatrix} j_1 \\ \vdots \\ j_n \end{pmatrix} = \begin{pmatrix} B_{x,1} \\ \vdots \\ B_{x,m} \end{pmatrix} \tag{9}$$

where n denotes the number of arc current lines, for this example $n = 8$. The element a_{ij} corresponds to the i-th measure due to the contribution of the j-th current value. And $a_{ij}$is only associated with the x coordinates of each node. Equation (9) can be expressed in the form

$$\boldsymbol{Aj} = \boldsymbol{b}, \tag{10}$$

where $\boldsymbol{A} \in \boldsymbol{R}^{m \times n}$ is the Biot-Savart operator matrix, $\boldsymbol{j}$ the vector composed of each current value, and $\boldsymbol{b}$ the vector composed of x-component magnetic field data measured at sampling points; note that $m > n$. Owing to the ill-posed property of operator matrix $\boldsymbol{A}$, in the sense that finding the solution of the equations is the least-squares solution, i.e., to solve $\boldsymbol{A}^*$, which satisfies

$$f(\boldsymbol{A}) = \|\boldsymbol{A}^*\boldsymbol{j} - \boldsymbol{b}\| = \inf_{A}\{\|\boldsymbol{Aj} - \boldsymbol{b}\| : \boldsymbol{A} \in \boldsymbol{F}\}, \tag{11}$$

where $\boldsymbol{F}$ represents the feasible region of the solutions. From Fig. 3 we know that $\boldsymbol{F} = \{x \in \boldsymbol{F} | 0 \le x \le 50\}$. To obtain the position and shape of the arc, the current distribution is taken as an initial value. We assume the total current is j_{tot} and that each current is assumed to be $j_i = j_{tot}/i$, where i denotes the number of current lines. The operator $\boldsymbol{A}$ can be determined from Eq. (11) by a nonlinear optimization process. Then, $\boldsymbol{A}$ is substituted into Eq. (10), yielding $\boldsymbol{Aj} = \boldsymbol{b}$. Considering the multiple parameters and nonlinear properties of the equations, we use the MPGA to find the optimization solution.

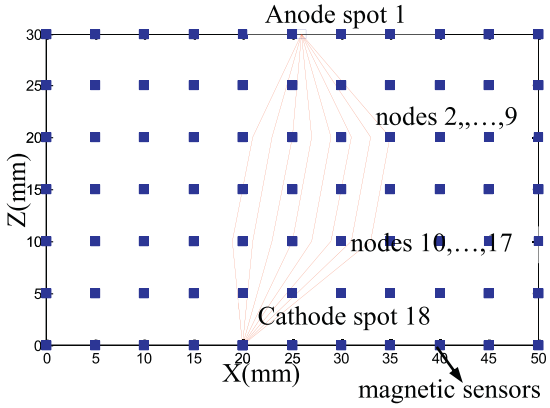

Fig. 3. Arc current line model and the magnetic sensor array.

Arc inversion by the nonlinear optimization

The MPGA

The Structure relationship among population of the MPGA is represented in Fig. 4. The parameters of the algorithm are set as follows, the population number $MP = 10$; the crossover probability of each population is generated randomly within [0.7, 0.9] and shown as

$$pc = 0.7 + (0.9 - 0.7) \cdot rand(MP, 1), \tag{12}$$

the mutation probability of each population is generated randomly within [0.001, 0.05] and shown as

$$pm = 0.001 + (0.05 - 0.001) \cdot rand(MP, 1), \tag{13}$$

the evolutionary generation $gen = 200$.

It should be noted that the position of each node $x_2, \ldots, x_9$ and $x_{10}, \ldots, x_{17}$ will be out of order in the optimization results. This is due to the non-uniqueness of the inversion. Thus, we define the penalty function $P(\boldsymbol{A})$ based on the position constraints among the nodes. The function $P(\boldsymbol{A})$ is expressed in (14), where $g(x_i, x_{i+1}) = x_{i+1} - x_i \ge 0$ and$h(x_i, x_{i+1}) = x_{i+1} - x_i \ge 0$are the node constraint functions. The objective functions are expressed as (15) by merging (11) and (14), where $\lambda = 1$ is the penalty coefficient:

$$P(\boldsymbol{A}) = \sum_{i=2}^{8} [\min(0, g(x_i, x_{i+1}))]^2 + \sum_{i=10}^{16} [\min(0, h(x_i, x_{i+1}))]^2, \tag{14}$$

$$f^*(\boldsymbol{A}) = f(\boldsymbol{A}) + \lambda P(\boldsymbol{A}). \tag{15}$$

Optimization results

To test the applicability of the proposed method, we apply the Gaussian noise to the calculated magnetic data to simulate the interference of the actual environment. The noise data $\boldsymbol{e}$ is shown as

$$\boldsymbol{e} = r \cdot std(\boldsymbol{b}) \cdot \boldsymbol{randn} \tag{16}$$

where $\boldsymbol{r} = 1\%$ denotes the signal-to-noise level, $std(\boldsymbol{b})$denotes the standard deviation of magnetic data $\boldsymbol{b}$, and $\boldsymbol{randn}$ is a random vectors from the standard normal distribution. With the noise imposed, the superimposed magnetic data can be expressed as$\boldsymbol{b} = \bar{\boldsymbol{b}} + \boldsymbol{e}$, in which $\bar{\boldsymbol{b}}$ denotes the pure data.

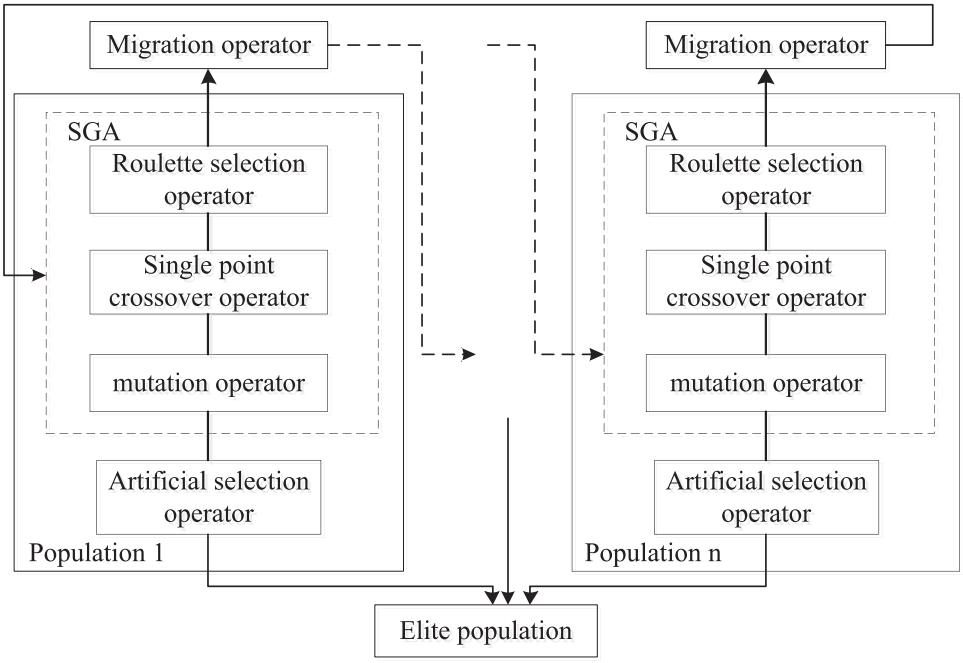

Fig. 4. Structure of MPGA

The evolution process of the objective function is shown in Fig. 5, compared with GA. The relative error for calculating the operator matrix $\boldsymbol{A}$ (i.e., the node positions x_1, x_2,…, x_{18}) is shown in Fig. 6.

It is observed from Fig. 5 that the MPGA converges to the optimal value faster than the GA. In Fig. 6, the maximum relative error of the MPGA for calculating the node positions is less than 15%, while it is 24% for the GA. Thus, it is proved that the MPGA has a certain precision and stability in optimizing multi-dimensional continuous functions. Therefore, we determined the coefficients, i.e. the matrix $\boldsymbol{A}$ in (10). In the next section, the current distribution is solved.

TGSVD for solving current distribution

Ill-posed equations

Based on the above work, the Biot-Savart operator $\boldsymbol{A}$ is obtained by the MPGA. $\boldsymbol{A}$ is then substituted into the original equation (10), and thus the over-determined linear system $\boldsymbol{A}_{m\times n}\boldsymbol{j} = \boldsymbol{b}_m$ is formed, where n denotes the number of current lines and m the number of sampling points, $m > n$.

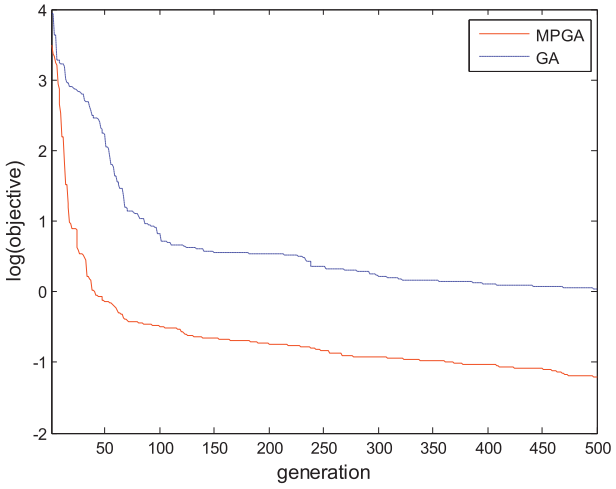

Fig. 5. MPGA and SGA evolution processes.

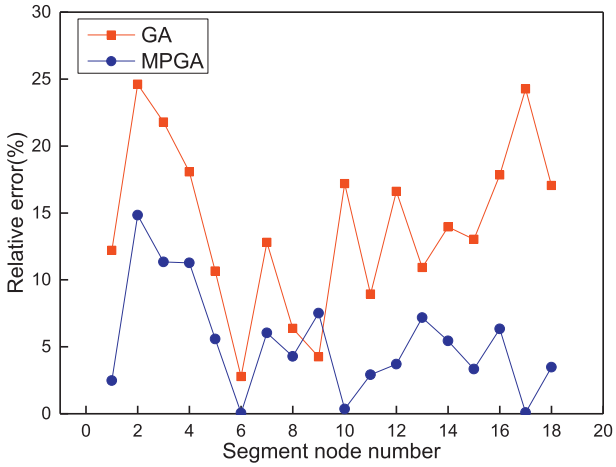

Fig. 6. Relative errors of MPGA and SGA.

The TGSVD method

To solve the ill-posed equation $\boldsymbol{Aj} = \boldsymbol{b}$, first, the SVD of the matrix $\boldsymbol{A} \in \boldsymbol{R}_r^{m\times n}$ can be expressed as

$$\boldsymbol{A} = \boldsymbol{U}\begin{pmatrix}\sum & 0\\ 0 & 0\end{pmatrix}\boldsymbol{V}^{\mathrm{T}} = \sum_{i=1}^{r}\sigma_i\boldsymbol{u}_i\boldsymbol{v}_i^{\mathrm{T}}, \tag{17}$$

where $\boldsymbol{U} = (\boldsymbol{u}_1, \ldots, \boldsymbol{u}_n)$ and $\boldsymbol{V} = (\boldsymbol{v}_1, \ldots, \boldsymbol{v}_n)$ are orthogonal matrices with orthonormal columns. $\Sigma = \mathrm{diag}(\sigma_1, \ldots\sigma_r)$ is the diagonal matrix in which $\sigma_1, \ldots\sigma_r$ are the positive singular values. Thus, the solutions of the equation $\boldsymbol{Aj} = \boldsymbol{b}$ can be represented as follows:

$$\boldsymbol{j} = \sum_{i=1}^{r}\frac{\boldsymbol{u}_i^{\mathrm{T}}\boldsymbol{b}}{\sigma_i}\boldsymbol{v}_i, \tag{18}$$

where $\boldsymbol{u}_i$ and $\boldsymbol{v}_i$ are the columns of the matrices $\boldsymbol{U}$ and $\boldsymbol{V}$, respectively. The matrix condition number is $cond(\boldsymbol{A}) = \sigma_{max}/\sigma_{min} = 564$, which is much larger than 1, suggesting that the operator $\boldsymbol{A}$ is ill-conditioned. This will result in a huge deviation on the solution $\boldsymbol{j}$ due to a small perturbation on the magnetic data $\boldsymbol{b}$. In many applications, TSVD regularization is used to improve the ill-posed properties of the operator $\boldsymbol{A}$ by truncating the $r-k$ small singular values, where k denotes the truncation parameter. The regularization solutions of TSVD are denoted

$$\boldsymbol{j}_k = \sum_{i=1}^{k} \frac{\boldsymbol{u}_i^{\mathrm{T}}\boldsymbol{b}}{\sigma_i}\boldsymbol{v}_i. \tag{19}$$

However, the data tend to be severely contaminated, resulting in the solutions of TSVD being insufficient to achieve high precision. To address this problem, we introduce the general form of TSVD, i.e., TGSVD. First, the generalized singular value decomposition (GSVD) of the matrix pair $(\boldsymbol{A}, \boldsymbol{L})$ is denoted

$$\boldsymbol{A} = \boldsymbol{U}\begin{pmatrix} \sum & 0 \\ 0 & \boldsymbol{I}_{n-p} \end{pmatrix}\boldsymbol{X}^{-1}, \quad \boldsymbol{L} = \boldsymbol{V}\begin{pmatrix} \boldsymbol{M} & 0 \end{pmatrix}\boldsymbol{X}^{-1}, \tag{20}$$

where $\boldsymbol{U} \in \boldsymbol{R}^{m\times n}$, $\boldsymbol{U}^{\mathrm{T}}\boldsymbol{U}=\boldsymbol{I}_n$ and $\boldsymbol{V} \in \boldsymbol{R}^{p\times p}$, $\boldsymbol{V}^{\mathrm{T}}\boldsymbol{V}=\boldsymbol{I}_p$ are column orthogonal matrices, and $\boldsymbol{X} \in \boldsymbol{R}^{n\times n}$ is a non-singular matrix. The $p \times p$ diagonal matrices $\boldsymbol{\Sigma}$ and $\boldsymbol{M}$ are denoted

$$\sum = diag(\sigma_i), \boldsymbol{M} = diag(\mu_i), \tag{21}$$

where the elements σ_i and μ_i satisfy

$$\sigma_i^2 + \mu_i^2 = 1, \tag{22}$$

$$0 \le \sigma_1 \le \ldots \le \sigma_p \le 1, 0 \le \mu_p \le \ldots \le \mu_1 \le 1. \tag{23}$$

The generalized singular values γ_i of the matrix pair $(\boldsymbol{A}, \boldsymbol{L})$ are defined as

$$\gamma_i = \frac{\sigma_i}{\mu_i}, i = 1, 2, \ldots, p. \tag{24}$$

The solutions of TGSVD for the problem $\boldsymbol{Aj} = \boldsymbol{b}$ are subsequently derived as

$$\boldsymbol{j}_{k,L} = \sum_{i=p-k+1}^{p} \frac{\boldsymbol{u}_i^{\mathrm{T}}\boldsymbol{b}}{\sigma_i}\boldsymbol{x}_i + \sum_{i=p+1}^{n} \boldsymbol{u}_i^{\mathrm{T}}\boldsymbol{b}\boldsymbol{x}_i, \tag{25}$$

where $\boldsymbol{x}_i$ is the i-th column of the matrix $\boldsymbol{X}$. We define the second term in (25) as

$$\boldsymbol{x}_0 = \sum_{i=p+1}^{n} \boldsymbol{u}_i^{\mathrm{T}}\boldsymbol{b}\boldsymbol{x}_i, \tag{26}$$

where $\boldsymbol{x}_i, i = p+1, \ldots, n$ are the basis vectors of the null space $N(\boldsymbol{L})$. Christensen-Dalsgaard [13] revealed that the ordinary singular vectors $\boldsymbol{v}_i$ from SVD have irregular undesired localized oscillations with increasing i, which are insufficient to produce smooth solutions. For the GSVD method, the regularization matrix $\boldsymbol{L}$ is related to the accuracy of the solution $\boldsymbol{j}_{k,L}$. In this case, we choose $\boldsymbol{L} \in \boldsymbol{R}^{p\times n}$ as the banded matrices $\boldsymbol{L}_1$ and $\boldsymbol{L}_2$, which are denoted

$$\boldsymbol{L}_1 = \begin{pmatrix} 1 & -1 & & \\ & \ddots & \ddots & \\ & & 1 & -1 \end{pmatrix}, \boldsymbol{L}_2 = \begin{pmatrix} 1 & -2 & 1 & & \\ & \ddots & \ddots & \ddots & \\ & & 1 & -2 & 1 \end{pmatrix}, \tag{27}$$

where $p = n-1$ and $n-2$, respectively. The matrices $\boldsymbol{L}_1$ and $\boldsymbol{L}_2$ have non-trivial null spaces $N(\boldsymbol{L})$. The regularization matrices $\boldsymbol{L}_1$ and $\boldsymbol{L}_2$ are the approximations to the first- and second-derivative operators,

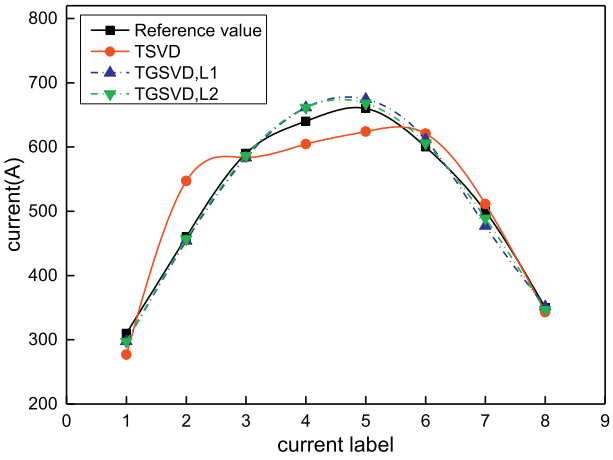

Fig. 7. Current reconstruction results.

respectively. It has been validated that if $\boldsymbol{L} = \boldsymbol{L}_2$, the singular vectors $\boldsymbol{x}_i$ in (25) display remarkably smoothness, totally unlike $\boldsymbol{v}_i$ obtained from SVD [13]. Moreover, the basis vectors of $N(\boldsymbol{L}_1)$and$N(\boldsymbol{L}_2)$are shown as

$$(1, 1, \ldots, 1)^{\mathrm{T}}, \tag{28}$$

$$(1, 1, \ldots, 1)^{\mathrm{T}}, (1, 2, \ldots, n)^{\mathrm{T}}, \tag{29}$$

which present no oscillations. They are included in the TGSVD solution and are not affected by the regularization process. This explains why the TGSVD method can get higher accuracy solution.

The truncation parameter k plays a key role in the quality of the solutions. It has been shown that the GCV criterion performed better than the other parameter selection strategies [10]. Thus we use the GCV criterion to select the truncation parameter. This method works by selecting k to minimize the following expression:

$$G(k) = \frac{\left\|\boldsymbol{Aj}_{reg} - \boldsymbol{b}\right\|_2^2}{(trace(\mathbf{I}_m - \boldsymbol{AA}^{reg}))^2}, \tag{30}$$

Where $\boldsymbol{j}_{reg} = \boldsymbol{j}_{k,L}$ denotes the regularized solution, $\boldsymbol{A}^{reg}$ the regularized inverse, i.e., $\boldsymbol{j}_{reg} = \boldsymbol{A}^{reg}\boldsymbol{b}$, $trace()$ denotes the diagonal sum of the matrix, and $\mathbf{I}_m$ the identity matrix.

Current reconstructed results

Fig. 7 shows the reconstructed current distribution of TSVD and TGSVD in the presence of the assumed noise signal with level $r = 1\%$. The reference distribution basically accords with the real distribution. The reconstructed current distributions inverted by the TGSVD method agree well with the reference distribution. Although the current distributions obtained by the TSVD method accord with the reference distribution in general, it deviates apparently from the reference distribution of the arc core area. In an actual environment, the measured magnetic data tend to be disturbed, which will cause more relative error. Thus, by replacing the regularization operator from the identity matrix to the banded matrix, the inversion process has a stronger ability to overcome the disturbance.

To evaluate the inversion results comprehensively, we introduce common evaluation parameters, signal-to-noise ratio (*SNR*) and mean square error (*MSE*), and defined as follows,

Table 1
Relative error of current-inverting results.

	Truncation parameter	*SNR*	*MSE*	δ_r(%)
TSVD	$k = 3$	22.73	1.49×10^3	7.31
TGSVD, $(\boldsymbol{L} = \boldsymbol{L}_1)$	$k = 2$	31.58	195.96	2.65
TGSVD, $(\boldsymbol{L} = \boldsymbol{L}_2)$	$k = 1$	34.10	109.52	1.98

$$SNR = 10\lg \frac{\|\boldsymbol{j}_{true}\|^2}{\|\boldsymbol{j}_{true} - \boldsymbol{j}_{rec}\|^2}, \tag{31}$$

$$MSE = \frac{1}{n}\|\boldsymbol{j}_{true} - \boldsymbol{j}_{rec}\|^2, \tag{32}$$

where $\boldsymbol{j}_{true}$denotes the reference current values, $\boldsymbol{j}_{rec}$denotes the reconstructed values, and n is the unknowns number of the equation, $\|\cdot\|$ denotes the Euclidean norm. The relative error δ_r is defined as follows.

$$\delta_r = \frac{\|\boldsymbol{j}_{err}\|}{\|\boldsymbol{j}_{true}\|} = \frac{\|\boldsymbol{j}_{rec} - \boldsymbol{j}_{true}\|}{\|\boldsymbol{j}_{true}\|} \tag{33}$$

According to Table 1, when the noise level $r = 1\%$, the *MSE* and δ_r of the TSVD method are much larger than those of TGSVD method, which indicates that the TSVD method is more sensitive to the noise than TGSVD. The *SNR* of the TSVD reconstruction result is lower than that of TGSVD, which further verifies the effectiveness of the TGSVD method. In addition, the TGSVD method with $\boldsymbol{L} = \boldsymbol{L}_2$ performed better than $\boldsymbol{L} = \boldsymbol{L}_1$. This shows that the reconstruction precision of $\boldsymbol{L}_2$ is sufficient in this case.

Conclusions

In this paper, an arc is assimilated to be a succession of current segments. This assumption simplifies the calculation complexity of the model. By combining the nonlinear optimization of the MPGA and linear regularization of TGSVD, the arc-inversion problem is solved by inverting the magnetic field data. The MPGA is more accurate and robust than GA in dealing with the arc-position inversion, and the current density reconstructed by TGSVD is consistent with the reference distribution. In the future, we plan to study a more precise arc model that is closer to an actual model, and will consider reducing the number of magnetic sensors to save the cost of the inversion process.

Conflict of interest

The author(s) declare no potential conflicts of interest with respect to the research, authorship, and/or publication of this article.

Acknowledgments

This work is supported by the National Natural Science Foundation of China under grant 51377106. We thank LetPub (www.letpub.com) for its linguistic assistance during the preparation of this manuscript.

References

[1] G. Kong, Z. Liu, D. Wang, M. Rong, High-current vacuum arc: the relationship between anode phenomenon and the average opening velocity of vacuum interrupters, IEEE Trans. Plasma Sci. 39 (6) (2011) 1370–1378.
[2] X. Li, D. Chen, H. Liu, Y. Chen, Z. Li, Imaging and spectrum diagnostics of air arc plasma characteristics, IEEE Trans. Plasma Sci. 32 (6) (2004) 2243–2249.
[3] D. Hong, G. Sandolache, J. Bauchire, F. Gentils, C. Fleurier, A new optical technique for investigations of low-voltage circuit breakers, IEEE Trans. Plasma Sci. 33 (2) (2005) 976–981.
[4] J.P. Toumazet, C. Brdys, A. Laurent, J.L. Ponthenier, Combined use of an inverse method and a voltage measurement: estimation of the arc column volume and its variations, Meas. Sci. Technol. 16 (16) (2005) 1525–1533.
[5] E. Debellut, F. Gary, D. Cajal, A. Laurent, Study of re-strike phenomena in a low-voltage breaking device by means of the magnetic camera, J. Phys. D Appl. Phys. 34 (11) (2001) 1665–1674.
[6] P. Zhang, G. Zhang, J. Dong, W. Liu, Y. Geng, Non-intrusive magneto-optic detecting system for investigations of air switching arcs, Plasma Sci. Technol. 16 (7) (2014) 661–668.
[7] J. Cochran, S. Horng, J. Fowler, A multi-population genetic algorithm to solve multi-objective scheduling problems for parallel machines, Comput. Oper. Res. 30 (7) (2003) 1087–1102.
[8] L. Li, Y. Tang, D. Pan, Design optimization of air-cored PMLSM with overlapping windings by multiple population genetic algorithm, IEEE Trans. Magn. 50 (11) (2014) 1–5.
[9] Q. Zhou, W. Luo, A novel multi-population genetic algorithm for multiple-choice multidimensional knapsack problems, in: Proceedings of the 5th International Conference on Advances in Computation and Intelligence, 2010, pp. 148–157.
[10] J. Dong, G. Zhang, Z. Zhang, Y. Geng, J. Wang, Inverse problem solution and regularization parameter selection for current distribution reconstruction in switching arcs by inverting magnetic fields, Math. Probl. Eng. (2018) 1–12.
[11] L. Ghezzi, D. Piva, L. Di Rienzo, Current density reconstruction in vacuum arcs by inverting magnetic field data, IEEE Trans. Magn. 48 (8) (2012) 2324–2333.
[12] P. Hansen, Regularization, GSVD and truncated GSVD, BIT Numer. Math. 29 (3) (1989) 491–504.
[13] J. Christensen-Dalsgaard, P. Hansen, M. Thompson, Generalized singular value decomposition analysis of helioseismic inversions, Mon. Not. R. Astron. Soc. 264 (3) (1993) 541–564.